ACS APPLIED MATERIALS & INTERFACES

Research Article

www.acsami.org

Flame-driven Aerosol Synthesis of Copper–Nickel Nanopowders and Conductive Nanoparticle Films

Munish K. Sharma,[†] Di Qi,[†] Raymond D. Buchner,[†] William J. Scharmach,[‡] Vasilis Papavassiliou,[‡] and Mark T. Swihart*,[†]

[†]Department of Chemical and Biological Engineering, The University at Buffalo (SUNY), Buffalo, New York 14260, United States

[‡]Praxair, Inc., 175 E Park Drive, Tonawanda, New York 14150, United States

Supporting Information

ABSTRACT: We report the continuous one-step synthesis of bimetallic copper–nickel nanostructured coatings by deposition and sintering of metal nanoparticles produced as an aerosol using a flame driven high temperature reducing jet (HTRJ) process. The HTRJ process allows gas-phase (aerosol) formation of metal nanoparticles from low-cost metal salt precursors. These can be collected as discrete powders for subsequent use in formulating conductive inks or for other applications. However, direct deposition of nanoparticles to form coatings allows measurements of electrical conductivity of films of deposited nanoparticles as a function of composition and sintering temperature, without actually formulating and printing inks. This is the approach taken here for the purpose of screening nanoparticle compositions quickly. We characterized the microstructure and composition of both nanopowders and films and found that their composition consistently matched the ratio of metals in the precursor solution. The electrical conductivity was highest (~10^4 S/m) for films with 60:40 and 40:60 copper-to-nickel mass ratios. These films maintained their conductivity during extended storage (1 month) under ambient conditions. The oxidation resistance and high conductivity observed here suggest that 60:40 and 40:60 Cu:Ni nanoparticles have promise as lower cost replacements for silver nanoparticles in conductive ink formulations.

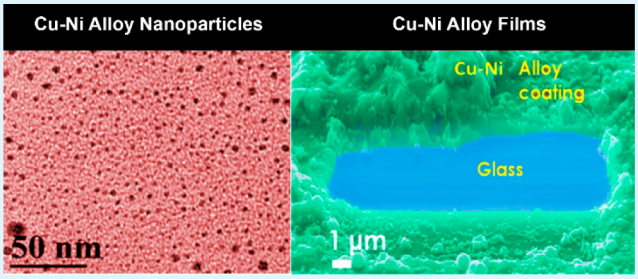

KEYWORDS: *nanoparticles, copper, nickel, sintering, conductivity*

INTRODUCTION

The synthesis of metallic nanoparticles is of great current interest and potential future industrial importance. Aerosol synthesis can provide a continuous, scalable, one-step approach to produce nanoparticles and nanoparticle-based coatings. Recent advances in aerosol reactor technology provide improved control of particle size, morphology, structure, and composition.[1,2] Various approaches for deposition of nanoparticles from an aerosol to produce a nanostructured film have been developed in recent years. Many of these are flame-based processes that rely on thermophoresis as the driving force for particle deposition. An et al. and Zhan et al. prepared thin films of SnO_2, NiO, and TiO_2 using an aerosol-chemical vapor deposition (ACVD) technique and flame aerosol reactor (FLAR).[3,4] Tolmachoff et al. used a rotating substrate to stabilize a premixed flame doped with a titania precursor and thereby deposited uniform nanoparticulate TiO_2 films on the rotating surface.[5] Zhang et al. similarly used a premixed swirl flame in a stagnation point geometry to deposit TiO_2 films, and provided a simplified deposition model to correlate deposition parameters and film morphology.[6] Sahm et al. used direct deposition from a flame-spray-pyrolysis process to produce pure and doped tin oxide nanoparticle films for gas sensor applications.[7] These flame-based processes have mostly been developed for metal oxide particles that can readily be produced in open flames. In contrast, production of nonoxide materials generally requires an enclosed system that can provide a reducing environment. Holman et al. and Anthony et al. have prepared silicon and germanium nanocrystals in a low-pressure plasma process and then deposited them by acceleration through a nozzle and impaction at low pressure.[8,9] In such processes, inertial impaction provides the driving force for film deposition. Kubo et al. produced metal oxide nanoparticles in a plasma and applied a positive bias to their substrate to enhance deposition of the negatively charged particles.[10] Varying particle generation and deposition conditions allowed them to control the porosity and structure of the films.

Considerable effort has been directed toward preparing nanopowders of metals such as silver and gold for printable and flexible electronics applications, due to their high electrical conductivity and resistance to oxidation at ambient conditions.[11−15] However, the high cost of silver and gold limits their use in metal ink formulations for low-cost high-volume applications. To address this concern, some researchers have

Received: May 2, 2014
Accepted: July 30, 2014
Published: July 30, 2014

investigated copper−nickel alloys.[16−18] Use of copper nanoparticles in metal ink formulations is limited by oxidation of copper to cuprous and cupric oxides (CuO/Cu_2O) with electrical conductivities characteristic of lightly doped *p*-type semiconductors ($\sim 10^{-2}/10^{-3}$ S/m).[11,19,20] Addition of nickel to copper improves its oxidation resistance.[20] Bulk copper−nickel alloys are used in applications such as shipbuilding and chemical process equipment in which they are exposed to harsh conditions such as marine environments, acid and alkaline media, and oxidative−reductive environments.[16,17,21−26] The corrosion resistance of Cu−Ni alloys is usually attributed to formation of a thin, strongly adherent inner barrier layer of Cu_2O that is in contact with a thicker outer layer of $Cu(OH)_2$. In the alloy, nickel migrates into the barrier layer of Cu_2O and fills cation vacancies, which leads to an increase in the corrosion resistance.[22,27] However, the applicability of this mechanism of corrosion resistance to nanostructured materials, and its effect on electrical conductivity of nanoparticle films, is not presently known.

The essential requirement for conductive inks is that they form films that exhibit electrical conductivity of at least 100 S/m after low-temperature sintering. Postprocessing of printed electronics usually includes a heating step that increases electrical conductivity. Immediately after printing, the conductivity can be low, due to oxidation, poor contact between particles, and the presence of surfactants and binders that are used to disperse the metal nanoparticles into a solvent to produce a stable and printable ink.[15,19] The maximum allowable temperature for heat treatment depends upon the thermal stability of the substrate used, but is often in the range of 200−250 °C for polymers such as polyethylene terephthalate (PET), polycarbonate (PC), and polypropylene (PP). These materials can be disfigured or degraded above 200 °C.[13,19,28,29] Therefore, reducing the postprocessing temperature by discovering and using new combinations of metals and alloys and manipulating their physical and surface properties is of great interest. Other sintering methods, such as laser sintering and flash annealing can reduce the thermal load on the substrate and provide improved sintering, relative to simple thermal sintering, but these also benefit from use of materials with lower sintering temperature. Thus, formulations that are optimal for thermal sintering should be near optimal for advanced sintering methods as well.

Prior studies have attempted synthesis of copper−nickel alloys via several methods. Jung et al. prepared Cu−Ni alloys directly from the metal salt solution via ultrasonic mist combustion and ultrasonic pyrolysis.[30] However, their product particles were contaminated with organic byproducts from the solvent and salt precursors. Cangiano et al. synthesized Cu−Ni alloys by a citrate-gel method and subsequent decomposition, calcination, and reduction.[21] Ahmed et al. have synthesized bimetallic Cu−Ni particles of varying composition such as $CuNi_3$, CuNi, and Cu_3Ni via a microemulsion route using CTAB (cetyltrimethylammonium bromide) as a surfactant and hydrazine as a reducing agent followed by reduction in a hydrogen atmosphere.[16] These methods all have key limitations such as difficulty of scale-up, prohibitively large energy input, or use of strong reducing agents and expensive surfactants to reduce the metal precursors and stabilize the metal nanoparticle dispersion. Therefore, new low-cost and scalable processes for synthesizing copper−nickel nanoparticles are still needed.

Here we demonstrate the preparation of copper−nickel nanoparticles and coatings by thermal decomposition of water-soluble nitrate precursors using the high temperature reducing jet (HTRJ) process.[31] The HTRJ process is a flame-based method in which liquid precursors are injected above the flame, within a converging−diverging nozzle. Acceleration of the hot combustion products through a nozzle provides atomization of the precursor and exceptionally rapid heating and mixing. The separation of the flame chemistry, upstream of the nozzle, from particle formation chemistry, downstream of the nozzle is advantageous for producing metal nanoparticles and differentiates the HTRJ process from most other flame-based aerosol synthesis methods. Use of excess hydrogen in the flame produces a reducing environment, allowing production of metals, rather than metal oxides, for elements that can be reduced by hydrogen in the presence of water. As shown in our previous studies, nonagglomerated particles are produced within the reactor.[31,32] These can be deposited directly onto a substrate placed at the reactor exit, where the hot aerosol leaving the reactor is mixed with cold quench gas. The substrate temperature is controlled by varying the quench gas flow rate. Like other flame-based processes, the deposition is mainly thermophoretically driven. The deposition occurs at roughly atmospheric pressure, and the particles are too small for impaction to play an important role. This contrasts with approaches where acceleration through a nozzle into a low-pressure region is used to deposit particles by impaction.[8,9] Here, we use this thermophoretic film deposition as a means of quickly screening different nanoparticle compositions without formulating and printing a nanoparticle-based ink for each composition. This provides a best-case scenario for electrical conductivity, because no binders or surfactants have to be removed from the films. Ultimately, the most promising compositions should be formulated into inks, printed, and annealed to fully assess their suitability as replacements for silver or other conductive ink components. In the present study, we are not aiming to demonstrate a practical process for producing films for actual use in printed electronics. Rather, we are interested in producing the nanoparticles and assessing their potential for use in structures printed by more conventional means. Alternatively, one could couple the HTRJ nanoparticle synthesis process to an aerosol-jet printing process that can print fine features directly. However, we have not attempted to do so.

Note that in this study, the nanoparticles are sintered in a hydrogen-containing reducing atmosphere in the reactor. Thus, oxidation during sintering is not expected. However, upon exposure to the atmosphere, oxidation can occur. Both pure Ni and pure Cu nanoparticles and nanostructured films oxidize under ambient conditions. The key point of the current study is to show that copper−nickel nanostructured films do not oxidize under ambient conditions over a 1 month period, in contrast to the pure Ni and pure Cu nanoparticles and films.

The copper−nickel nanoparticles and nanoparticulate coatings were characterized using scanning electron microscopy (SEM), transmission electron microscopy (TEM), and powder X-ray diffraction (XRD). In addition, we studied the effect of oxygen flow rate on the particle size and degree of crystallinity. Varying the oxygen flow supplied to the HTRJ reactor changes the combustion temperature and hence the temperature at which the particles form. The oxidation resistance of copper−nickel coatings was studied by measuring changes in electrical conductivity in the nanoparticulate films over a period of 1 month of storage at ambient laboratory conditions.

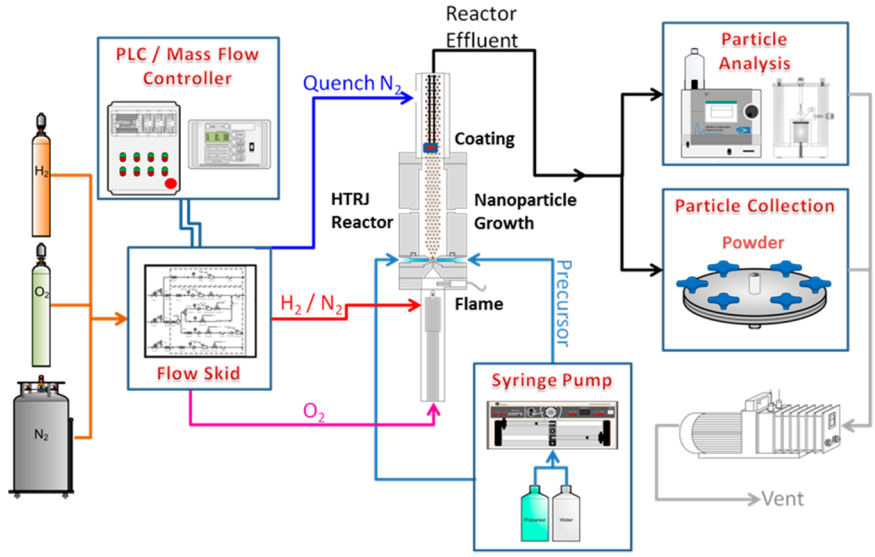

Figure 1. Overall schematic illustration of high temperature reducing jet reactor (HTRJ) reactor system.

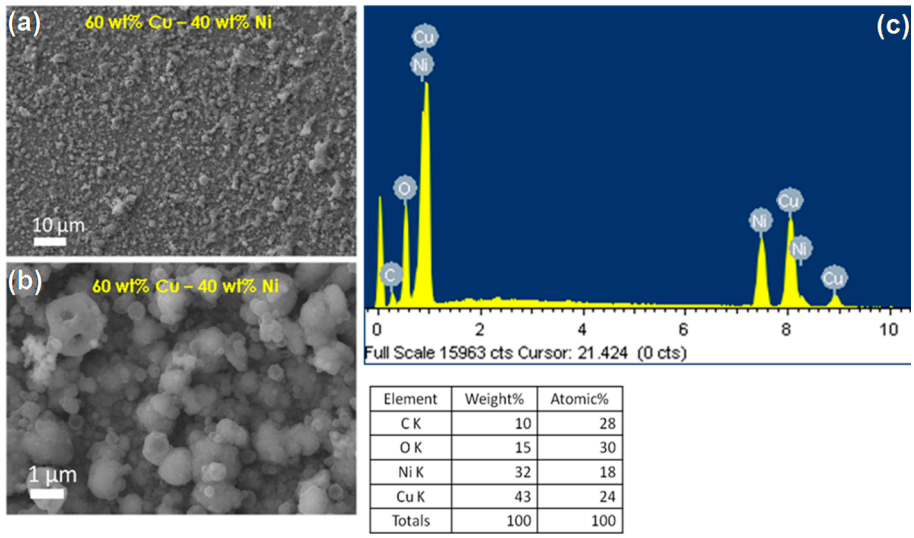

Element	Weight%	Atomic%
C K	10	28
O K	15	30
Ni K	32	18
Cu K	43	24
Totals	100	100

Figure 2. Detailed characterization of copper–nickel coating deposited on a glass substrate from precursors with 60 wt % Cu, 40 wt % Ni; (a) low magnification SEM image of Cu–Ni coating; (b) higher magnification SEM image of Cu–Ni coating; (c) EDS analysis of copper–nickel coating, indicating the presence of Cu and Ni. The normalized (metals only) composition was 57 wt % Cu–43 wt % Ni.

EXPERIMENTAL SECTION

Figure 1 shows an overall schematic of the high temperature reducing jet reactor system used in this study. It was previously described in detail by Scharmach et al.[31] In it, oxygen gas at a flow rate of ~2.3 standard liters per minute (SLM) and a larger flow of hydrogen and nitrogen (~14 SLM total) support an inverted diffusion flame. Excess hydrogen is always used (H_2-to-O_2 ratio of ~3.9), so the flame temperature depends primarily on the oxygen flow rate. The system is insensitive to the exact H_2 flow rate, provided that H_2 is in significant excess and the total H_2 plus N_2 flow remains constant. The hot combustion products are accelerated through a converging–diverging nozzle. The aqueous precursor solution is delivered into the throat of the nozzle by four small symmetrically arranged inlets. The high-velocity hot gas stream atomizes the precursor solution, which rapidly evaporates and decomposes, producing metal or metal oxide particles. Any oxides formed are reduced to the corresponding metals by the excess hydrogen present in the system. Precursors used in these experiments included copper nitrate hemipentahydrate (ACS reagent, ≥98.0%, Acros Organics) and nickel nitrate hexahydrate (99%, Acros Organics). For all experiments reported here, the aqueous precursor solution had a total metal concentration of 10 mM and was supplied at a flow rate of 180 mL/h. Nanoparticles were collected using a 293 mm diameter Durapore brand polyvinylidene fluoride (PVDF) membrane filter with 0.22 μm pore size. This provides efficient particle collection with minimal pressure drop at the flow rates used here. Nanostructured coatings were deposited on 12.5 mm diameter glass windows (Edmund Optics). A single deposition substrate (window) was mounted perpendicular to the gas flow, on the reactor axis, just above the reactor exit. The substrate temperature was measured with a thermocouple touching the back side of the aluminum SEM sample stub upon which the glass window was mounted. The measured temperature was ~200 °C. For all films presented in this paper, the total coating time was 3 h.

The copper and nickel nanopowder and coatings were analyzed by a series of methods, including X-ray diffraction (XRD) (Rigaku Ultima IV X-ray diffractometer), transmission electron microscopy (TEM) (JEOL JEM 2010 at an accelerating voltage of 200 kV), and scanning electron microscopy (AURIGA CrossBeam Workstation (FIB-SEM) from Carl Zeiss SMT) with an Oxford Instruments X-Max 20 mm^2 EDS detector and INCA software for elemental composition determination. A custom-built electrostatic sampler, similar to that

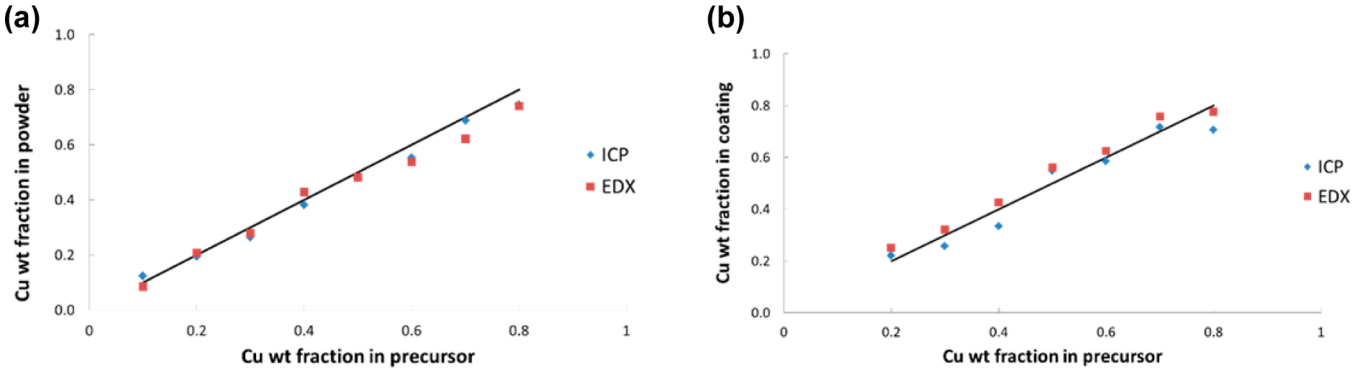

Figure 3. Compositional analysis of copper−nickel powders and coatings using ICP and EDS. Plots show copper mass fraction in (a) powders and (b) deposited films, as a function of copper mass fraction in the precursor solution, as measured using ICP-OES (blue diamonds) and EDS (red squares).

described by Dixkens and Fissan,[33] was used for collecting particles directly onto TEM grids for offline analysis. For bulk electrical conductivity of coatings, a four point probe was used with a Keithley 2400 sourcemeter. An atomic force microscope (AFM) with a camera scan head (Nanosurf Easyscan 2) was used to image the copper−nickel coatings and determine their thickness and root-mean-square (RMS) roughness. A scanning mobility particle sizer (SMPS) consisting of an ultrafine condensation particle counter (UCPC, TSI Model 3776) coupled with a short differential mobility analyzer (DMA, TSI model 3085), a high voltage power supply (Bertan Model 205 B-10 R), and a home-built ^{210}Po neutralizer was used to measure electrical-mobility-based particle size distributions. For this, a small fraction of the reactor effluent was diverted and diluted with cold nitrogen before entering the SMPS, while the majority of the flow still passed through the collection filter. An inductively coupled plasma-optical emission spectrometry system (iCAP 6000 series ICP-OES, Thermo Scientific) was used to determine the composition of both powders and coatings.

RESULTS AND DISCUSSION

In this study, we varied the precursor solution composition to achieve copper-to-nickel ratios from 1:9 to 9:1, while keeping the total metal ion concentration in solution constant at 10 mM. The sintering temperature of the coatings in all cases was fixed at ∼200 °C. Here, we present complete characterization results for a coating of only one composition, Cu (60 wt %)−Ni (40 wt %), which was one of the compositions exhibiting the highest electrical conductivity. Figure 2 shows SEM images and results of elemental analysis by EDS for this film. Figure 2a shows a low magnification SEM image of the coating and Figure 2b shows a higher magnification SEM image of the coating, which demonstrates that it is nonuniform and sintered. The table in Figure 2c shows the overall composition measured by EDS including carbon and oxygen, which are always found in these porous films after exposure to ambient conditions. Oxygen can also arise from oxides of copper and nickel formed upon exposure of the films to air. The SiO_2 substrate could also contribute, but no Si signal is seen. Although the 30 atom % O may seem high for a conductive film, it is not unusual in such high surface area materials, which can adsorb a substantial quantity of water on their surface. The carbon signal in the spectrum at the top surface of the film was not detected in the interior of the film, and is attributed to ubiquitous carbon contamination from atmospheric exposure. The metal mass fraction of Cu in the precursor solution was 0.60, and that measured by EDS in the film was 0.57 (normalized fraction considering only metals). These are equal to within the uncertainty of the EDS measurements. This illustrates the capability of the HTRJ process to provide accurate control over the composition of bimetallic coatings by completely converting the precursors to particles.

Composition of nanopowders and coatings was measured using both inductively coupled plasma atomic emission spectroscopy (ICP-OES) and EDS. The nanopowder collected downstream on the filter paper was characterized using EDS and the copper-to-nickel ratio was computed, excluding other elements. ICP-OES was used for more accurate determination of elemental composition in the nanopowder and coatings. For ICP-OES measurements, a known mass of copper−nickel powder or coating was dissolved in aqueous nitric acid. To compare EDS and ICP analysis, the same set of compositions were chosen for both powder and coating. As shown in Figure 3, the mass fraction of copper in copper−nickel powders and coatings is in good agreement between the two characterization methods. Moreover, the nanopowder and film compositions match the elemental ratios in the precursor. In Figure 3, the black lines represent the composition that would be expected if the ratio in the coating or powder were identical to that in the copper−nickel precursor mixture, and the product compositions are consistently close to this line. This demonstrates the composition control provided by the HTRJ process, which results from the complete conversion of precursors into product particles. The close match between precursor composition, deposited film composition, and collected particle composition also provides evidence that film formation is dominated by nanoparticle deposition, and that chemical vapor deposition (CVD) processes are not making a major contribution to film growth. In most CVD processes, the deposition efficiencies of different elements (from different precursors) are not the same, and therefore the elemental ratios in the film do not generally match the elemental ratios in the precursors.

Elemental mapping was done using EDS to determine the distribution of copper and nickel in the coating, as shown in Figure 4. Figure 4a shows an SEM image of a 60 wt % Cu−40 wt % Ni coating. EDS maps of copper and nickel, indicating a uniform distribution of both elements over the entire scanned region are shown in Figure 4b,c. This confirms the ability of the HTRJ process to synthesize uniformly mixed coatings. We estimated the coating thickness by tilting the sample and milling through the entire thickness of the coating using a focused ion beam (FIB), then measuring the thickness via SEM. Figure 4d shows an SEM image of the coating from which the

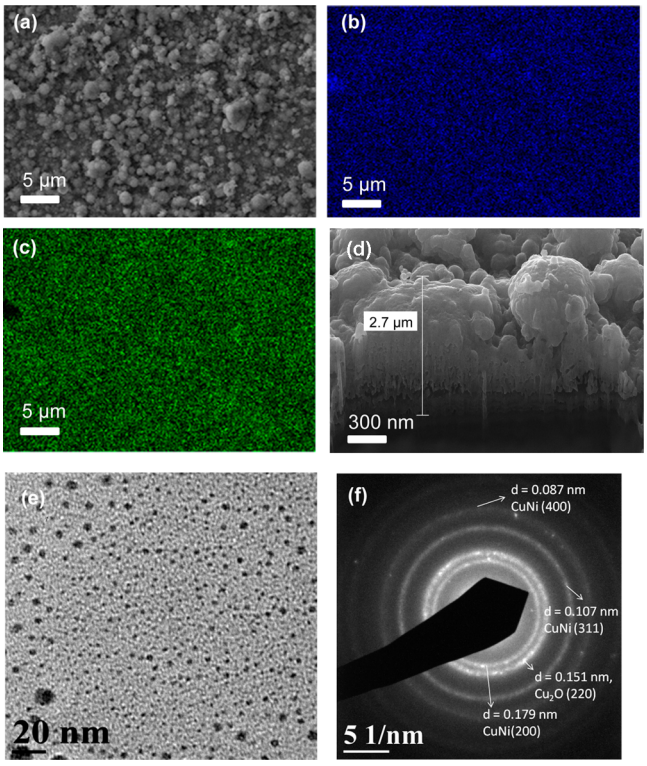

Figure 4. Detailed characterization of copper−nickel coating and nanoparticles with 60 wt % Cu, 40 wt % Ni composition; (a) low magnification SEM image of Cu−Ni coating; (b) EDS map of copper; (c) EDS map of nickel; (d) SEM image showing thickness and internal structure of coating; (e) representative TEM image of copper−nickel nanoparticles; (f) SAED pattern of copper−nickel nanoparticles.

film thickness was roughly estimated to be 2.7 μm (taking into account viewing angle correction). This image also shows that the internal structure of the film is relatively dense and nonporous, reflecting substantial restructuring of the deposited particles by sintering. This indicates that the film morphology is not governed by the nanoparticle deposition mechanism, but by the dynamics of sintering after deposition. Deposition without significant sintering or restructuring would produce a highly porous film (typically >80% porosity).

Figure 4e shows a transmission electron microscope (TEM) image of representative copper−nickel nanoparticles collected by electrostatic deposition directly onto a TEM grid. Figure 4f shows a selected area electron diffraction (SAED) pattern of these nanoparticles, with diffraction from CuNi and Cu_2O crystals, as labeled. The nanoparticles seen in TEM images (e.g., Figure 4e) are much smaller than the structures visible in SEM images (Figure 4a). As discussed further below, the sizes observed in TEM are consistent with size distribution measurements made using a scanning mobility particle spectrometer. Thus, we attribute the formation of larger structures to postdeposition sintering and restructuring of the film. Such larger structures can also be formed directly by droplet-to-particle conversion. We have previously observed this phenomenon under nonoptimal reactor operating conditions (e.g., precursor flow rate too large or pressure ratio across the nozzle too high or too low), and the resulting large, hollow, spherical particles are quite obvious in both SEM and TEM images. That was not the case for the experiments reported here.

To determine the relative distribution of copper and nickel along the thickness of the coatings, an EDS line scan was made along the thickness of the coating after the coating was milled (Figure S3 in the Supporting Information). The copper-to-nickel ratio was constant along the depth profile, indicating that neither element segregated to the surface of the film. Unfortunately, due to the lower sensitivity of EDS to light elements, we were not able to obtain comparable depth profiles for carbon and oxygen. Qualitatively, the carbon signal disappeared within the film, and the oxygen signal decreased.

A more accurate determination of the average coating thickness was made using atomic force microscopy (AFM), as shown in Figure S4 (Supporting Information). The thickness was calculated by scratching the coating across the diameter of the substrate and measuring the Δz (depth) between the glass and coating at different locations perpendicular to the scratch, over a 50 × 50 μm^2 square area and then averaging to give a mean thickness of 1.06 μm. AFM measurement also yielded a root-mean-square roughness value (R_q) of 458 nm.

The mixed copper−nickel particles and coatings were also analyzed by powder X-ray diffraction. The overlaid XRD patterns of nanopowders (collected on a filter downstream of the reactor) prepared using various copper−nickel ratios in the precursor solution are shown in Figure 5a. Peaks in the XRD patterns can be assigned to copper, nickel, copper−nickel alloys, and the corresponding oxides. Reference patterns are shown below the experimental patterns. The presence of multiple phases and the possibility of changes in lattice constant due to alloying make the peak assignments somewhat ambiguous. Reitveld refinement was applied to several of the patterns, but in most cases, unique fits were not obtained, i.e., different combinations of phase fractions and crystallite sizes could produce comparably good fits to the data. Nonetheless, the oxide-related peaks and metal-related peaks are sufficiently separated to provide insight into the degree of oxidation and most likely phases present in each case. Copper-rich and nickel-rich samples both showed substantial oxidation, consistent with the propensity of pure copper and pure nickel to oxidize under ambient conditions. However, in the composition range of 40 to 60 wt % Ni, oxidation-resistant copper−nickel alloy nanoparticles were formed, and the degree of oxidation was much reduced, as shown by the strong CuNi (111) peak in the XRD patterns. Figure 5b shows XRD data for the copper and nickel coatings prepared by depositing nanoparticles directly onto a glass substrate at ∼200 °C. The alloying of copper and nickel is demonstrated by the CuNi (111) peak at 2θ = 44.85°, corresponding to a d-spacing of 2.06 Å, intermediate between the copper (111) d-spacing of 2.08 Å and nickel (111) d-spacing of 2.04 Å. Although this small difference in lattice spacing would be difficult, if not impossible, to resolve in real-space measurements (i.e., HRTEM), such differences are easily resolved in XRD. The 40 wt % Cu−60 wt % Ni and 60 wt % Ni−40 wt % Ni XRD patterns show the highest degree of alloying with a more pronounced CuNi (111) peak compared with the other compositions. Comparing the results for the powders in Figure 5a with those for the films in Figure 5b, we see that the CuNi alloy peak in the films is more prominent (relative to the other peaks), indicating a greater degree of alloying in the films than in the powder. This is consistent with the occurrence of alloying along with sintering in the films, which is to be expected since Cu and Ni are miscible, i.e., form solid solutions at all compositions in the bulk.

dx.doi.org/10.1021/am5026853 | ACS Appl. Mater. Interfaces 2014, 6, 13542−13551

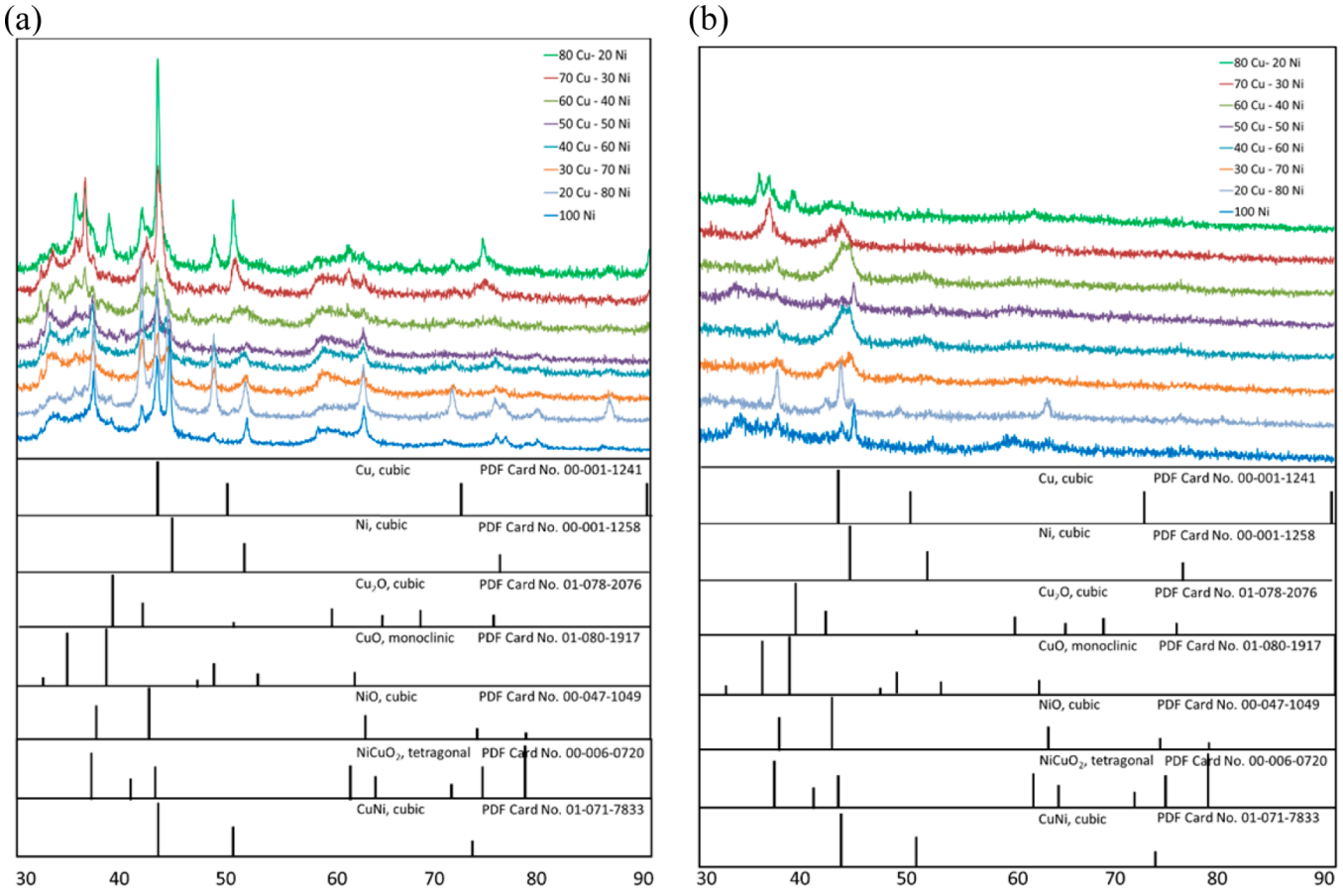

Figure 5. Powder X-ray diffraction of copper−nickel (a) powders collected downstream of reactor and (b) coatings on glass substrates, with varying composition (wt %).

The flame that provides the energy input to the HTRJ process is an inverted diffusion flame (oxidant-O_2 on the inside, fuel-H_2 on the outside). The flame temperature is controlled by varying the oxygen flow, while always using excess hydrogen. To determine the effect of reactor temperature on particle size, and the effects of crystallite size on electrical conductivity of coatings, three oxygen flow rates were tested: 2.0, 2.3, and 2.6 SLPM. This varied the particle size produced in the reactor. The approximate temperature at the surface of the particle formation chamber was monitored using a K-type thermocouple and was found to be 350, 400, and 430 °C for oxygen flows of 2.0, 2.3, and 2.6 SLPM. The temperature along the reactor centerline is expected to be substantially higher, but correlated with this measured temperature. The adiabatic flame temperatures for these three sets of gas flow rates are approximately 1960, 2185, and 2395 °C. Heat flow to the reactor walls, cooling due to expansion through the converging−diverging nozzle, and cooling due to evaporation of the precursor solution result in a temperature in the particle formation chamber that is substantially below the adiabatic flame temperature, although the temperature upstream of the nozzle may approach the adiabatic flame temperature. Computational fluid dynamics modeling suggests that the temperature within the particle formation chamber is relatively uniform and is 800 to 1000 °C below the adiabatic flame temperature, but still more than 300 °C above the near-wall temperature measured by the thermocouple.[34] The sintering temperature of Cu−Ni coatings was kept at ∼200 °C in all the three cases by varying the quench nitrogen gas flow rate to compensate for the changes in reactor temperature. We measured electrical mobility based size distributions using a scanning mobility particle sizer, as shown in Figure 6. The geometric mean and geometric standard deviation were measured to be d_g = 7.8 nm, σ_g = 1.6 for 2.0 SLPM, d_g = 9.4 nm, σ_g = 1.6 for 2.3 SLPM, and d_g = 10.2 nm, σ_g = 1.7 for 2.6 SLPM oxygen flow rates, respectively. The geometric mean

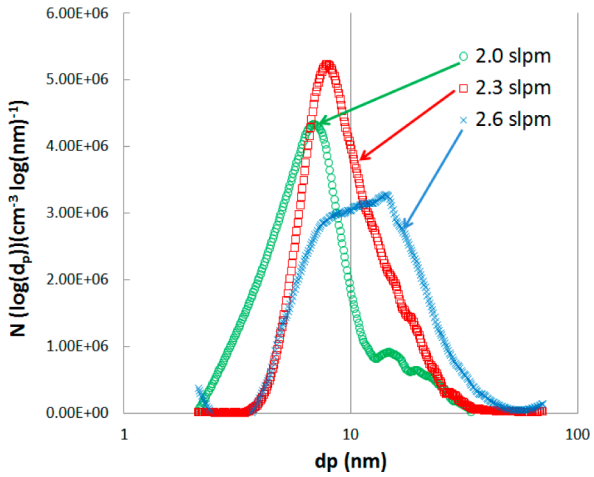

Figure 6. Particle size distribution as measured using a scanning mobility particle sizer (SMPS) for 60 wt % copper, 40 wt % nickel particles at 2.0, 2.3, and 2.6 SLPM oxygen flow rates.

dx.doi.org/10.1021/am5026853 | ACS Appl. Mater. Interfaces 2014, 6, 13542−13551

diameter was calculated from SMPS data by the usual definition: $\ln(d_g) = (\sum n_i * \ln(d_i))/(\sum n_i)$, where d_g is geometric mean diameter and n_i is the number of particles in the size range centered at diameter d_i. A higher reactor temperature produces slightly larger nanoparticles. The size distributions from the SMPS are generally consistent with the size range observed in TEM images of particles collected directly from the aerosol onto a TEM grid in the electrostatic precipitator.

At each oxygen flow rate, surface characterization of coatings was carried out using SEM and EDS. Phase and crystallite size determination using powder X-ray diffraction were also carried out for the three different conditions. Bulk electrical conductivity of Cu−Ni coatings was measured 1 day after synthesis. Figure 7 shows SEM micrographs of coatings

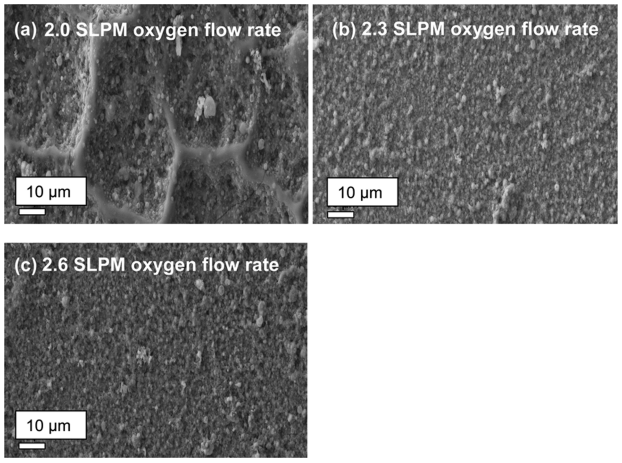

Figure 7. Scanning electron microscopy images of copper−nickel (60 wt % Cu−40 wt % Ni composition) coatings produced at (a) 2.0 SLPM, (b) 2.3 SLPM, and (c) 2.6 SLPM oxygen flow rates.

produced at 2.0, 2.3, and 2.6 SLPM oxygen flow rates. The film prepared using 2.0 SLPM oxygen appears somewhat smoother compared to those produced using 2.3 or 2.6 SLPM O_2. All other things being equal, the sintering rate increases strongly with decreasing particle size. For the most common sintering mechanisms, characteristic sintering time scales as diameter to the fourth power.[35,36] Thus, the small changes in the diameter of deposited particles can potentially produce substantial changes in sintering dynamics.

To characterize the crystallite size for the three conditions, powder X-ray diffraction was carried out on coatings (Figure S5 in the Supporting Information). Crystallize size was calculated by fitting the XRD pattern (Reitveld refinement) assuming one copper−nickel alloy phase (cubic $Ni_{0.4}Cu_{0.6}$) and one mixed oxide phase (tetragonal $NiCuO_2$), as shown in Figure S5 in the Supporting Information. The crystallite size dependence on oxygen flow rate is shown in Figure 8. The crystallite size for the 60 wt % Cu−40 wt % Ni coating for 2.3 and 2.6 SLPM oxygen flow rate was similar, at 11 nm, but the crystal size for 2.0 SLPM oxygen was smaller, at 5.5 nm. The crystallite sizes obtained in the film are comparable to the particle sizes measured by SMPS, suggesting that little grain growth occurs during sintering of the films. The electrical conductivity was also measured for Cu−Ni coatings synthesized at 2.0, 2.3, and 2.6 SLPM oxygen flow rates. The average conductivity from two independent runs is shown on a semilog plot in Figure 8. The conductivity measurements for two independent batches were in reasonable agreement, with differences between two

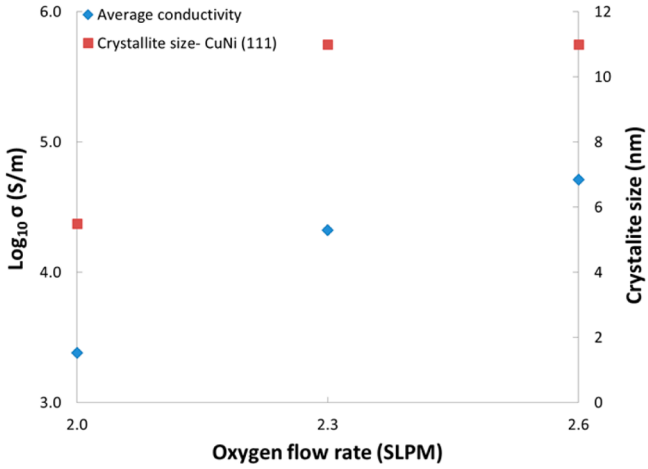

Figure 8. Crystallite size calculated by fitting XRD patterns (Reitveld refinement) and electrical conductivity (in S/m, on a $\log_{10}$ scale) for copper−nickel (60 wt % Cu−40 wt % Ni) films as a function of oxygen flow rate.

batches of 5%, 2%, and 24% for the three oxygen flow rates. The electrical conductivity of the Cu−Ni coating at 2.3 and 2.6 SLPM oxygen flow rate was of the order of 10^4 S/m, whereas the conductivity of the film prepared at 2.0 SLPM was 1 order of magnitude lower. The increased conductivity at higher oxygen flow rates could result from larger crystallite size and lower density of grain boundaries. The phase fraction of oxide obtained by fitting of the XRD patterns was also notably higher for the film produced at 2.0 SLM compared to the other two films (Figure S5, Supporting Information).

As discussed above, bulk copper−nickel alloys are quite oxidation resistant. Whether this remains the case at the microscale and nanoscale is less clear. To assess effects of oxidation over time, the electrical conductivity of coatings was measured after varying periods of air exposure, under ambient laboratory conditions ($T \approx 20$ °C and $P \approx 1$ atm). Electrical conductivity was measured after 1 day, 1 week, 2 weeks, 3 weeks, and 4 weeks of storage time. The variation of electrical conductivity (on a log scale) against nickel wt % over a period of 1 month is shown in Figure 9. We found that electrical conductivity of films containing 30−80 wt % Ni was quite stable over time. The bulk electrical conductivity of pure copper is 6×10^7 S/m at 293 K, but pure copper nanostructured films oxidized immediately in the presence of air. The conductivity of our copper films sintered at 200 °C was of order 10^{-2} S/m, consistent with the formation of semiconducting copper oxides.[37,38] The bulk conductivity of nickel is 1.4×10^7 S/m at 293 K, but it is also prone to oxidation and the conductivity of our nickel nanostructured films fell to 10^{-1} S/m, which is just 1 order of magnitude higher than that of the oxidized copper nanoparticulate film. Makhlouf et al. studied the electrical conductivity of NiO films of varying thickness and found that for a film thickness of 2 μm, electrical conductivity was near 10^{-3} S/m.[39] Starting from pure copper, and then increasing the nickel content, the conductivity increased up to 40 wt % Ni−60 wt % Cu, where the conductivity reached a maximum at 10^5 S/m, which is one to 2 orders of magnitude lower than the conductivity of bulk copper and nickel, and 3 orders of magnitude above the minimum conductivity required for most printed electronics applications. At 50 wt % Cu−50 wt % Ni, we observed a small decrease in conductivity, to ~10^4 S/m. At 60 wt % Ni−40 wt % Cu, conductivity rose to a higher

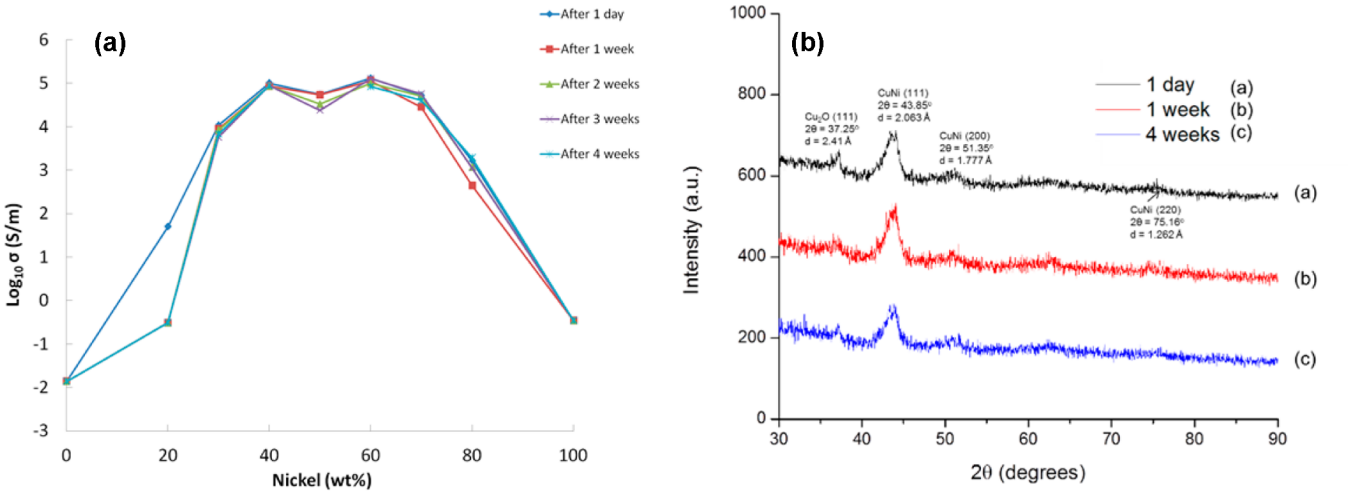

Figure 9. (a) Electrical conductivity of copper−nickel coatings as a function of nickel content and storage time (under exposure to air at ambient lab conditions). (b) Overlay of XRD patterns of 60 wt % Cu−40 wt % Ni coatings as a function of storage time.

value of 1.3 × 10^5 S/m. Further increasing the Ni content reduced the conductivity. Cu−Ni films with 40 wt % Ni−60 wt % Cu and 60 wt % Ni−40 wt % Cu compositions therefore show the greatest promise for use as replacements for silver in metal ink formulations. Powder X-ray diffraction was done to detect oxidation of coatings as a function of time. The XRD analysis for the 40 wt % Cu−60 wt % Ni coating is presented in Figure 9. The CuNi alloy (111) diffraction peak at 2θ = 43.85° is the most prominent feature. The intensity of the small Cu_2O peak at 2θ = 37.25° remains constant over the storage time. This shows that most of the copper oxidation in the coating occurred during the first day, and no further oxidation is evident. Although thin passivating layers of oxide might not be detectable by XRD, the lack of change in both the electrical conductivity and the XRD patterns together provides evidence that the films are not oxidizing under ambient laboratory conditions.

In comparison with our previous studies of metal nanoparticles produced with the HTRJ process, we found that the size of Cu−Ni nanoparticles produced here was similar to that of Cu−Ag nanoparticles produced under similar conditions. Moreover, we found a similarity in the surface morphology of both Cu−Ag and Cu−Ni bimetallic systems as seen in SEM images. In that case, films were rough and the presence of copper and silver oxides was confirmed using XRD. The RMS value of surface roughness for a Cu−Ag coating measured by AFM was 450 nm with an average thickness of 1.25 μm. For Cu−Ni, the RMS roughness was measured to be 458 nm and an average thickness of 1.06 μm, for identical synthesis conditions and deposition time. This shows that the HTRJ system is capable of reproducing metal/metal oxide films with similar morphology and thickness and is independent of the metal system.

CONCLUSIONS

We demonstrated the production of copper−nickel nanopowders and nanostructured coatings using the flame-based HTRJ reactor. The size of copper and nickel nanoparticles prepared in this process was below 20 nm, based on both online SMPS and offline TEM analysis. This small size allows them to sinter at relatively low temperatures. Direct deposition of nanostructured coatings with in situ sintering at about 200 °C allowed us to test the composition dependence of the conductivity of sintered particle films without any intermediate processing steps such as ink formulation and spin-coating or printing. Nanostructured coatings with 40 wt % nickel−60 wt % copper and 60 wt % nickel−40 wt % copper had electrical conductivity that exceeds requirements for virtually all conductive thin film or printed electronic applications where silver-based inks are presently used. This high conductivity is retained even when these films are exposed to air for a period of one month. Thus, the oxidation resistance of bulk copper−nickel alloys is maintained in these nanopowders and nanostructured films, as demonstrated via XRD analysis and electrical conductivity measurements. Moreover, the composition of copper−nickel powders and coatings consistently matched the composition of copper and nickel in the precursor solution, demonstrating the simplicity of controlling composition in this process, and suggesting that the precursors are fully converted to the product particles. The HTRJ flame-based process allows continuous production of these multicomponent nanopowders using low-cost water-soluble metal salt precursors and could thereby provide a low cost route to such materials.

ASSOCIATED CONTENT

Supporting Information

Energy dispersive X-ray spectra and EDS elemental maps of nanopowder from precursors with 60 wt % Cu−40 wt % Ni. Depth profile of copper and nickel content of milled film. AFM images used in determining film thickness and roughness. XRD patterns of films produced at different oxygen flow rates with Reitveld refinement to determine crystallite sizes and phase fractions. This material is available free of charge via the Internet at http://pubs.acs.org.

AUTHOR INFORMATION

Corresponding Author

*Mark T. Swihart. E-mail: swihart@buffalo.edu. Tel.: +1-716-645-1181.

Notes

The authors declare no competing financial interest.

■ ACKNOWLEDGMENTS

This work was supported by the U.S. National Science Foundation (grant CBET-0652042). We thank Dr. Yueling Qin, University at Buffalo Integrated Nanostructured Systems Instrumentation Facility for help with TEM and FIB imaging.

■ REFERENCES

(1) Athanassiou, E. K.; Grass, R. N.; Stark, W. J. Chemical Aerosol Engineering as a Novel Tool for Material Science: From Oxides to Salt and Metal Nanoparticles. *Aerosol Sci. Technol.* **2010**, *44*, 161−172.
(2) Buesser, B.; Pratsinis, S. E. Design of Nanomaterial Synthesis by Aerosol Processes. *Annu. Rev. Chem. Biomol. Eng.* **2012**, *3*, 103−127.
(3) An, W.-J.; Thimsen, E.; Biswas, P. Aerosol-Chemical Vapor Deposition Method For Synthesis of Nanostructured Metal Oxide Thin Films With Controlled Morphology. *J. Phys. Chem. Lett.* **2010**, *1*, 249−253.
(4) Zhan, Z.; Wang, W.-N.; Zhu, L.; An, W.-J.; Biswas, P. Flame Aerosol Reactor Synthesis of Nanostructured SnO_2 Thin Films: High Gas-Sensing Properties by Control of Morphology. *Sens. Actuators, B* **2010**, *150*, 609−615.
(5) Tolmachoff, E. D.; Abid, A. D.; Phares, D. J.; Campbell, C. S.; Wang, H. Synthesis of Nano-phase TiO_2 Crystalline Films over Premixed Stagnation Flames. *Proc. Combust. Inst.* **2009**, *32*, 1839−1845.
(6) Zhang, Y. Y.; Li, S. Q.; Deng, S. L.; Yao, Q.; Tse, S. D. Direct Synthesis of Nanostructured TiO_2 Films with Controlled Morphologies by Stagnation Swirl Flames. *J. Aerosol. Sci.* **2012**, *44*, 71−82.
(7) Sahm, T.; Rong, W. H.; Barsan, N.; Madler, L.; Friedlander, S. K.; Weimar, U. Formation of Multilayer Films for Gas Sensing by in Situ Thermophoretic Deposition of Nanoparticles from Aerosol Phase. *J. Mater. Res.* **2007**, *22*, 850−857.
(8) Anthony, R. J.; Cheng, K.-Y.; Holman, Z. C.; Holmes, R. J.; Kortshagen, U. R. An All-Gas-Phase Approach for the Fabrication of Silicon Nanocrystal Light-Emitting Devices. *Nano Lett.* **2012**, *12*, 2822−2825.
(9) Holman, Z. C.; Kortshagen, U. R. A Flexible Method for Depositing Dense Nanocrystal Thin Films: Impaction of Germanium Nanocrystals. *Nanotechnology* **2010**, *21*, 9.
(10) Kubo, M.; Ishihara, Y.; Mantani, Y.; Shimada, M. Evaluation of the Factors that Influence the Fabrication of Porous Thin Films by Deposition of Aerosol Nanoparticles. *Chem. Eng. J.* **2013**, *232*, 221−227.
(11) CRC Handbook of Chemistry and Physics, 92 ed.; Haynes, W. M., Ed.; CRC Press (an imprint of Taylor & Francis Group): Boca Raton, FL. 2011.
(12) Cheon, J. M.; Lee, J. H.; Song, Y.; Kim, J. Synthesis of Ag Nanoparticles Using an Electrolysis Method and Application to Inkjet Printing. *Colloids Surf., A* **2011**, *389*, 175−179.
(13) Gamerith, S.; Klug, A.; Scheiber, H.; Scherf, U.; Moderegger, E.; List, E. J. W. Direct Ink-Jet Printing of Ag-Cu Nanoparticle and Ag-precursor based Electrodes for OFET Applications. *Adv. Funct. Mater.* **2007**, *17*, 3111−3118.
(14) Grouchko, M.; Kamyshny, A.; Magdassi, S. Formation of Air-Stable Copper-Silver Core-Shell Nanoparticles for Ink-Jet Printing. *J. Mater. Chem.* **2009**, *19*, 3057−3062.
(15) Grouchko, M.; Kamyshny, A.; Mihailescu, C. F.; Anghel, D. F.; Magdassi, S. Conductive Inks with a "Built-In" Mechanism That Enables Sintering at Room Temperature. *ACS Nano* **2011**, *5*, 3354−3359.
(16) Ahmed, J.; Ramanujachary, K. V.; Lofland, S. E.; Furiato, A.; Gupta, G.; Shivaprasad, S. M.; Ganguli, A. K. Bimetallic Cu-Ni Nanoparticles of Varying Composition ($CuNi_3$, CuNi, Cu_3Ni). *Colloids Surf., A* **2008**, *331*, 206−212.
(17) Ban, I.; Stergar, J.; Drofenik, M.; Ferk, G.; Makovec, D. Synthesis of Copper-Nickel Nanoparticles Prepared by Mechanical Milling for use in Magnetic Hyperthermia. *J. Magn. Magn. Mater.* **2011**, *323*, 2254−2258.
(18) Caglar, U.; Pekkanen, V.; Valkama, J.; Mansikkamaki, P.; Pekkanen, J.Usability of Ink-jet Printing Technology and Nanomaterials in Electrical Interconnections, Electronic Packaging, and System Integration for Microelectronics Applications. In *Ceramic Integration and Joining Technologies: From Macro to Nanoscale*; Singh, M., Ohji, T., Asthana, R., Mathur, S., Eds.; Wiley: New York, 2011; pp 743−776.
(19) Kamyshny, A.; Steinke, J.; Magdassi, S. Metal-based Ink Jet Inks for Printed Electronics. *Open Appl. Phys. J.* **2011**, *4*, 19−36.
(20) Chen, S.; Brown, L.; Levendorf, M.; Cai, W.; Ju, S.-Y.; Edgeworth, J.; Li, X.; Magnuson, C. W.; Velamakanni, A.; Piner, R. D.; Kang, J.; Park, J.; Ruoff, R. S. Oxidation Resistance of Graphene-coated Cu and Cu/Ni Alloy. *ACS Nano* **2011**, *5*, 1321−1327.
(21) de los, A.; Cangiano, M.; Carreras, A. C.; Ojeda, M. W.; del C. Ruiz, M. A New Chemical Route to Synthesize Cu-Ni Alloy Nanostructured Particles. *J. Alloys Compd.* **2008**, *458*, 405−409.
(22) Guo, F.; Lu, T.; Qin, J.; Zheng, H.; Tian, X. Abnormal Resistivity Behavior of Cu-Ni and Cu-Co Alloys in Undercooled Liquid State. *Phys. B (Amsterdam, Neth.)* **2012**, *407*, 4108−4113.
(23) Mohan, S.; Rajasekaran, N. Influence of Electrolyte pH on Composition, Corrosion Properties and Surface Morphology of Electrodeposited Cu-Ni Alloy. *Surf. Eng.* **2011**, *27*, 519−523.
(24) Khadom, A. A.; Yaro, A. S.; Kadhum, A. A. H. Adsorption Mechanism of Benzotriazole for Corrosion Inhibition of Copper-Nickel Alloy in Hydrochloric Acid. *J. Chil. Chem. Soc.* **2010**, *55*, 150−152.
(25) Ghauri, I. M.; Afzal, N.; Shahzad, M.; Mubarik, F. E. Tensile Behavior of Post-irradiation Annealed Cu-Ni Alloy. *Radiat. Eff. Defects Solids* **2011**, *166*, 228−232.
(26) Metikos-Hukovic, M.; Babic, R.; Skugor Roncevic, I.; Grubac, Z. Corrosion Resistance of Copper-Nickel Alloy under Fluid Jet Impingement. *Desalination* **2011**, *276*, 228−232.
(27) Metikos-Hukovic, M.; Babic, R.; Skugor, I.; Grubac, Z. Copper-Nickel Alloys Modified with Thin Surface Films: Corrosion Behaviour in the Presence of Chloride Ions. *Corros. Sci.* **2010**, *53*, 347−352.
(28) Polavarapu, L.; Manga, K. K.; Yu, K.; Ang, P. K.; Cao, H. D.; Balapanuru, J.; Loh, K. P.; Xu, Q.-H. Alkylamine Capped Metal Nanoparticle "Inks" for Printable SERS Substrates, Electronics and Broadband Photodetectors. *Nanoscale* **2011**, *3*, 2268−2274.
(29) Oehlund, T.; Oertegren, J.; Forsberg, S.; Nilsson, H.-E. Paper Surfaces for Metal Nanoparticle Inkjet Printing. *Appl. Surf. Sci.* **2012**, *259*, 731−739.
(30) Jung, C.-H.; Lee, H.-G.; Kim, C.-J.; Bhaduri, S. B. Synthesis of Cu-Ni Alloy Powder Directly from Metal Salts Solution. *J. Nanopart. Res.* **2003**, *5*, 383−388.
(31) Scharmach, W. J.; Buchner, R. D.; Papavassiliou, V.; Pacouloute, P.; Swihart, M. T. A High-Temperature Reducing Jet Reactor for Flame-based Metal Nanoparticle Production. *Aerosol Sci. Technol.* **2010**, *44*, 1083−1088.
(32) Sharma, M. K.; Buchner, R. D.; Scharmach, W. J.; Papavassiliou, V.; Swihart, M. T. Creating Conductive Copper-Silver Bimetallic Nanostructured Coatings Using a High Temperature Reducing Jet Aerosol Reactor. *Aerosol Sci. Technol.* **2013**, *47*, 858−866.
(33) Dixkens, J.; Fissan, H. Development of an Electrostatic Precipitator for off-Line Particle Analysis. *Aerosol Sci. Technol.* **1999**, *30*, 438−453.
(34) Sharma, M. K. Flame-based Synthesis of Multicomponent Metal Nanoparticles and Nanostructured Coatings. Ph.D. Dissertation, State University of New York at Buffalo, 2013.
(35) Chen, C. L.; Lee, J. G.; Arakawa, K.; Mori, H. Comparative Study on Size Dependence of Melting Temperatures of Pure Metal and Alloy Nanoparticles. *Appl. Phys. Lett.* **2011**, *99*, 013108/1−013108/3.
(36) Levitas, V. I.; Samani, K. Size and Mechanics Effects in Surface-Induced Melting of Nanoparticles. *Nat. Commun.* **2011**, *2*, 1275/1−1275/6.
(37) Young, A. P.; Schwartz, C. M. Electrical Conductivity and Thermoelectric Power of Cuprous Oxide. *J. Phys. Chem. Solids* **1969**, *30*, 249−252.

(38) Patil, A. U.; Sawant, S. R.; Powar, J. I.; Khot, A. Y.; Patil, R. N. Electrical Conductivity of Copper Oxide Thin Films at Microwave Frequencies. *Proc. Nucl. Phys. Solid State Phys. Symp.* **1978**, *21C*, 266.
(39) Makhlouf, S. A. Electrical Properties of NiO Films Obtained by High-Temperature Oxidation of Nickel. *Thin Solid Films* **2008**, *516*, 3112−3116.